Nano Res (2010) 3: 235–243
DOI 10.1007/s12274-010-1026-0
Research Article

Shape-Controlled Synthesis of Mn_3O_4 Nanocrystals and Their Catalysis of the Degradation of Methylene Blue

Pengqu Zhang[1], Yonggong Zhan[1,2] (✉), Bingxin Cai[1] (✉), Chenchun Hao[1], Jun Wang[1], Chunxiao Liu[1], Zhoujun Meng[1], Zhoulan Yin[2], and Qiyuan Chen[2]

[1] College of Chemistry and Chemical Engineering, Hunan University, Changsha 410082, China
[2] College of Chemistry and Chemical Engineering, Central South University, Changsha 410083, China

Received: 26 November 2009 / Revised: 28 January 2010 / Accepted: 29 January 2010

ABSTRACT

Various sizes and shapes of Mn_3O_4 nanocrystals have been prepared in a one-pot synthesis in extremely dilute solution by soft template self-assembly. To better control size and shape, the effects of varying the growth time, reaction temperature, surfactant, and manganese source were examined. The average size of octahedral Mn_3O_4 crystallites was found to be related to the reaction time, while higher reaction temperature (150 ˚C) and the use of a cetyltrimethylammonium bromide/poly(vinylpyrrolidone) (CTAB/PVP) mixture allowed construction of a better-defined octahedral morphologies. When PVP or poly(ethylene oxide)-poly(propylene oxide) (P123) was used as template, large-scale agglomeration resulting in loss of the octahedral morphology occurred and crystallites with a quasi-spherical shape were obtained. The nano-octahedral crystallites were shown to be an efficient catalyst for the oxidation of methylene blue.

KEYWORDS

Mn_3O_4, octahedron, nanocrystals, self-assembly, methylene blue

1. Introduction

Mn_3O_4, one of the most stable oxides of manganese, has tremendous potential in a large number of applications, such as catalysis [1–6], electrode materials [7, 8], and magnetic storage devices [9]. In particular, materials fabricated on a nanoscale can exhibit better phonic, optical, magnetic, thermal, and electrical properties than bulk materials. Hence, morphology-controllable syntheses of Mn_3O_4 nanomaterials have been investigated in detail, due to the morphology- and size-dependent properties of the resulting materials. A number of morphology-controllable synthetic methods for fabrication of nanostructured Mn_3O_4 have been reported; for example, reverse-micellar precipitation [10], thermal decomposition [11–15], templating processes [1, 7, 16–18], sol-gel processes [19–21], template-free routes [22], polyol-mediated, and chelation-mediated synthesis [8, 23]. However, no morphology-controllable methods for preparation of Mn_3O_4 nanocrystals have been reported for any system with extremely low precursor concentrations.

In this paper, we report a one-pot synthesis of various sizes and shapes of Mn_3O_4 crystallites using surfactants as structure-directing agents. Cetyltrimethylammonium

Address correspondence to Yonggong Zhan, ygzhan2006@yahoo.com.cn; Bingxin Cai, cbx@hnu.cn

bromide (CTAB), poly(vinylpyrrolidone) (PVP), and poly(ethylene oxide)-poly(propylene oxide) (P123) were used as surfactants and manganese sulfate ($MnSO_4·H_2O$), manganese chloride ($MnCl_2·4H_2O$), and a Mn–oleate complex were used as manganese sources. In our synthesis strategy, the key to controlling the morphology and structure was the rate of hydrolysis of the manganese precursors. From the perspective of chemical reaction kinetics, the reaction rate is largely dependent on the precursor concentration. A slow reaction rate was ensured by an extremely low precursor concentration under static conditions, and the interaction between the as-obtained nuclei and templates then formed the products. At the same time, an appropriate precipitant controlled the rate of hydrolysis of the manganese oxide precursor. In this system, urea was used as the precipitant to gradually release hydroxyl ions at the appropriate reaction temperature. It is well known that decomposition of urea affords ammonia and carbon dioxide [24–27], followed by the release of OH^- ions by hydrolysis of the ammonia solution. Simultaneously, the oxidation of a portion of Mn^{2+} to Mn^{3+} took place due to oxygen in the air, and the color of the solution changed from colorless to red-brown. The reaction processes occurring in air can be formulated as shown in Reactions 1, 2, and 3. The reaction conditions were altered in order to tune the rate of nucleation.

$$(NH_2)_2CO \longrightarrow NH_3 + CO_2 \quad (1)$$

$$Mn^{2+} + nNH_3 \longrightarrow Mn(NH_3)_n^{2+} \quad (2)$$

$$6Mn(NH_3)_n^{2+} + O_2 + 12OH^- \longrightarrow 2Mn_3O_4 + 6H_2O + 6nNH_3 \quad (3)$$

2. Experimental

2.1 Reagents and materials

Cetyltrimethylammonium bromide (CTAB, AR), manganese sulfate ($MnSO_4·H_2O$, AR), manganese chloride ($MnCl_2·4H_2O$, AR), urea (AR), cyclohexane (AR), benzyl alcohol (AR), poly(vinylpyrrolidone) (PVP, M_w = 10 000), poly(ethylene oxide)-poly(propylene oxide) (P123, M_w = 8400), sodium oleate (AR), and ethanol (AR), were all purchased from Sinopharm Chemical Reagent Co., Ltd. and used as received without further purification. Deionized water was used in all experiments.

2.2 Materials characterization

Scanning electron microscopy (SEM) images were obtained on (a) JSM-6700F instrument at 5 kV. Transmission electron microscopy (TEM) and high-resolution transmission electron microscopy (HRTEM) images were obtained on a JEM-3010F instrument at 200 kV. The samples were first ultrasonically dispersed in ethanol for 30 min and then were collected using copper grids covered with amorphous carbon films for TEM analysis and with a gold coating for SEM analysis. Powder X-ray diffraction (XRD) patterns were recorded with a Bruker D8-Advance diffractometer equipped with a Cu $K\alpha_1$ radiation source (λ = 1.541Å, 40 kV, 40 mA) with a step width of 0.01° (2θ) and an acquisition time of 4 s per step. For Raman measurements, a confocal microprobe Raman instrument (RamLab-010, HORIBA Jobin Yvon, France) was used. A 632.8-nm He–Ne laser excitation (0.1 mW) and a 50× long working-distance objective (8 mm) were used. The width of the slit and the size of the pinhole were set as 100 μm and 1000 μm, respectively. Absorption spectra was measured with a Lab Tech UV-2100 ultraviolet–visible (UV–Vis) spectrophotometer. The degradation products of methylene blue (MB dye) were analyzed by ICS3000 ion chromatography (Dionex Company, America).

2.3 Synthesis of Mn–oleate complex

The Mn–oleate complex was prepared as described in Ref. [28]. A 7.9164 g portion of manganese chloride tetrahydrate ($MnCl_2·4H_2O$, 40 mmol,) and 24.36 g of sodium oleate (80 mmol) were added to a mixture of 30 mL of ethanol, 40 mL of distilled water, and 70 mL of *n*-hexane. The resulting mixture was heated to 70 °C and maintained at this temperature for 4 h. The solution was then transferred to a separating funnel, and the upper organic layer containing the Mn–oleate

complex was washed several times using distilled water. Evaporation of the hexane solvent produced a brown powder of Mn–oleate complex.

2.4 Preparation of octahedral Mn_3O_4

In a typical procedure, 0.1800 g (5.6 mmol/L) $MnSO_4{\cdot}H_2O$, 1.3347 g (111.1 mmol/L) urea, and 1.2148 g (16.7 mmol/L) CTAB were added to 200 mL of water in a 250-mL conical flask, and the mixture was dissolved under magnetic stirring for 5 min. It was placed in a Teflon flask and kept at a thermostatically controlled temperature of 85 ˚C for one day under static conditions. The resulting red-brown precipitate was washed with 50 mL of ethanol and dried at 85 ˚C. Finally, the as-obtained Mn_3O_4 nanocrystals were calcined at 400 ˚C for 4 h to remove the surfactant.

2.5 Catalytic oxidation process

The catalytic reaction was carried out in a 250-mL glass flask, which contained 20 mL of MB dye solution (100 mg/L), 65 mL of distilled water, and 20 mg of catalyst. After adding 15 mL of 30 wt.% H_2O_2 solution, the mixture was allowed to react at 80 ˚C with continuous stirring. At given time intervals, 1 mL aliquots of the mixture were pipetted into a volumetric flask and quickly diluted with distilled water to 25 mL prior to analysis.

3. Results and discussion

The Mn_3O_4 nanocrystals prepared using a urea concentration of 111.1 mmol/L in the presence of CTAB (16.7 mmol/L) had an average crystallite size of 301 nm. SEM images (Fig. 1(a)) indicated that the shape of the resulting nanocrystals was almost octahedral, but they are tetragonally distorted due to the Jahn–Teller effect on Mn^{3+} ions [29]. Edge-shared [MnO_6] octahedral units [8, 30, 31] originate from the reaction at the nonbridging hydroxyl groups of adjacent micellar particle surfaces and form a chemical bond. Their construction results in agglomeration of most of the nanocrystals. As shown in Figs. 1(b) and 1(d) the crystallites show a well-fabricated octahedral morphology, similar to the idealized views in Figs. 1(c) and 1(e). The distance between two neighboring vertices is about 450 nm. The morphology and structure were further investigated by TEM and HRTEM. Low-resolution TEM (Fig. 1(g)) revealed the Mn_3O_4 to have an average crystallite size of 300–400 nm. Energy dispersive X-ray (EDX) spectroscopic analysis (Fig. 1(f)) confirmed that the crystallites consisted solely of

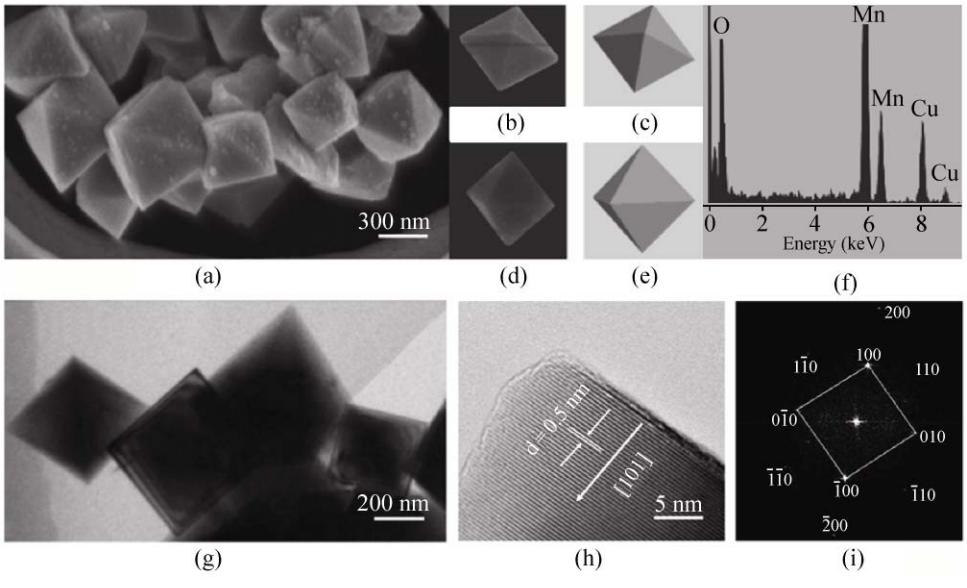

Figure 1 SEM images of octahedral structures: (a) low-magnification; (b) top view; (d) side view; (c) and (e) schematic illustrations of the octahedra; (f) energy dispersive X-ray (EDX) spectroscopic analysis; (g) TEM image; (h) high-resolution TEM image; (i) Fourier transform image of octahedral-structured Mn_3O_4 synthesized in the presence of $MnSO_4$ (5.6 mmol/L) and CTAB (16.7 mmol/L) at 85 ˚C for 24 h

manganese and oxygen, with a ratio that agreed well with the composition Mn_3O_4. The distinct lattice fringes observed in the HRTEM images (displayed in Fig. 1(h)) were about 0.5 nm, corresponding to the (101) reflections of Mn_3O_4, which confirmed the single crystallinity of the tetragonal phase Mn_3O_4 nanocrystal structures. Fast Fourier transform (FFT) of the lattice-resolved image (Fig. 1(i)) obtained from the HRTEM could also be indexed to a tetragonal Mn_3O_4 structure.

Wide-angle X-ray powder diffraction (XRD) patterns (Fig. 2(a)) showed diffraction peaks at 17.9°, 29°, 31°, 32.4°, 36.1°, 38°, 44.5°, 50.9°, 53.9°, 56°, 58.5°, 59.8°, 64.6°, and 74.6°, which can be indexed to the tetragonal structure of Mn_3O_4 (hausmannite structure, $I41/amd$) with lattice constants a = 5.746 Å and c = 9.463 Å. These values are consistent with the literature values for bulk Mn_3O_4 (JCPDS Card No.24-0734, a = 5.7621 Å and c = 9.4696 Å). However, Mn_3O_4 and γ-Mn_2O_3 have very similar structures and unit cell parameters and often co-exist [2], and cannot be easily discriminated by X-ray diffraction alone. The Raman spectra of the nanocrystals were therefore recorded, as shown in Fig. 2(b). Bands at 285, 315, 370, 472, and 655 cm^{-1} are consistent with those reported in the literature for Mn_3O_4 rather than Mn_2O_3 [1].

It was found that both kinetic control of the reaction conditions—such as varying the growth time, temperature, urea and monomer concentrations—as well as the choice of surfactant, could be used to tailor the morphologies and structures of the nanocrystals and control their growth rate. Figures 3(a)–3(d) shows SEM images of samples taken at different stages from a synthesis where the molar ratio of CTAB to $MnSO_4 \cdot H_2O$ was 3. When the hydrolysis took place at a temperature of 75 °C [32], only an amorphous morphology was apparent in the SEM images (Fig. 3(a)). As the reaction temperature was increased to 85 °C (Fig. 3(b)), the amorphous morphology gradually evolved into octahedral nanoparticles about 140 nm in size. After treatment at 150 °C for 8 h (Fig. 3(c)), the samples consisted of incomplete octahedral nanoparticles with particle size distribution shown by the histogram in (Fig. 4(a)) and an average crystallite size of 152 nm. Over the following 8 h at 150 °C (Fig. 3(d)), most of the well-defined octahedral nanoparticles grew to an average of 238 nm (Fig. 4(b)) in size. When the aging time at 150 °C was extended to 24 h (Fig. 4(c)), the nanoparticle size further increased to an average of 390 nm. The average crystallite size was therefore clearly dependent on the aging time and the process leading from incomplete octahedra to well-defined nanoparticles is probably due to Ostwald ripening [33, 34]. Since the hydrolysis rate of urea is known to depend on the reaction temperature, lower reaction temperatures (75 °C) were unable to provide the minimum surface energy needed for the

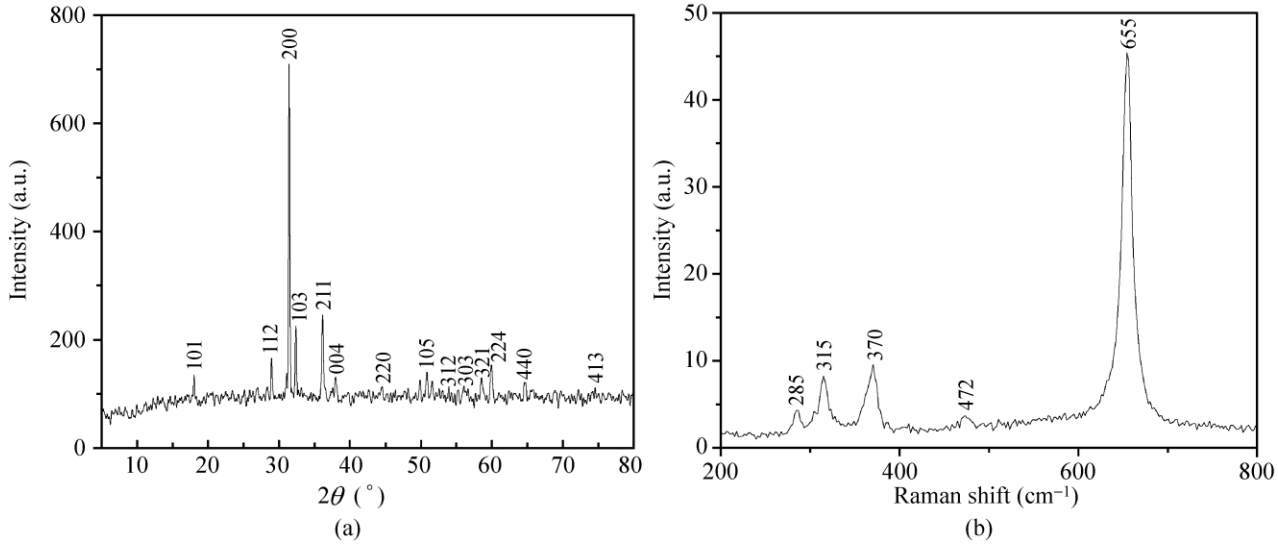

Figure 2 (a) XRD pattern, (b) Raman spectrum of Mn_3O_4 with $MnSO_4$ (5.6 mmol/L) and CTAB (16.7 mmol/L) at 85 °C for 24 h

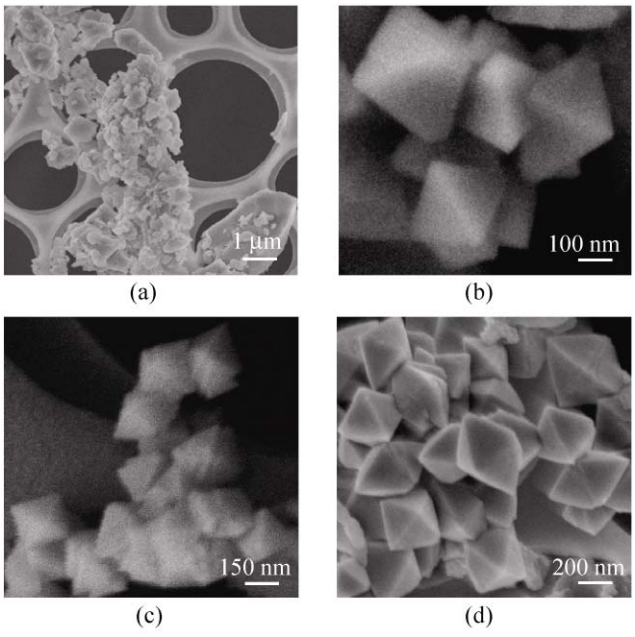

Figure 3 SEM images of products sampled at different stages of a synthesis: (a) 75 ˚C, (b) 85 °C, (c) 150 ˚C for 8 h, and (d) 150 ˚C for 16 h with $MnSO_4$ (5.6 mmol/L) and CTAB (16.7 mmol/L)

formation of an octahedron, whereas when a higher reaction temperature was chosen, crystallites with a better overall morphology were obtained. This was because the faster urea hydrolysis rate due to the increased reaction temperature released OH^- ions more quickly. These rapidly interacted with Mn^{2+}, thus avoiding the high surface energies that would result in agglomeration.

The presence of a CTAB/PVP mixture in the system played a key role in the formation of well-defined octahedral Mn_3O_4 nanocrystals. Large-scale agglomeration occurred in the presence of CTAB alone (Fig. 5(a), [CTAB] = 33.4 mmol/L), showing that it is not suitable for dispersing the particles at lower temperatures. For this reason, we altered the reaction conditions in order to ensure the formation of nanocrystals with well-constructed octahedral shapes. After mixing CTAB and PVP with a concentration ratio of 185.6, the nanocrystals became incorporated

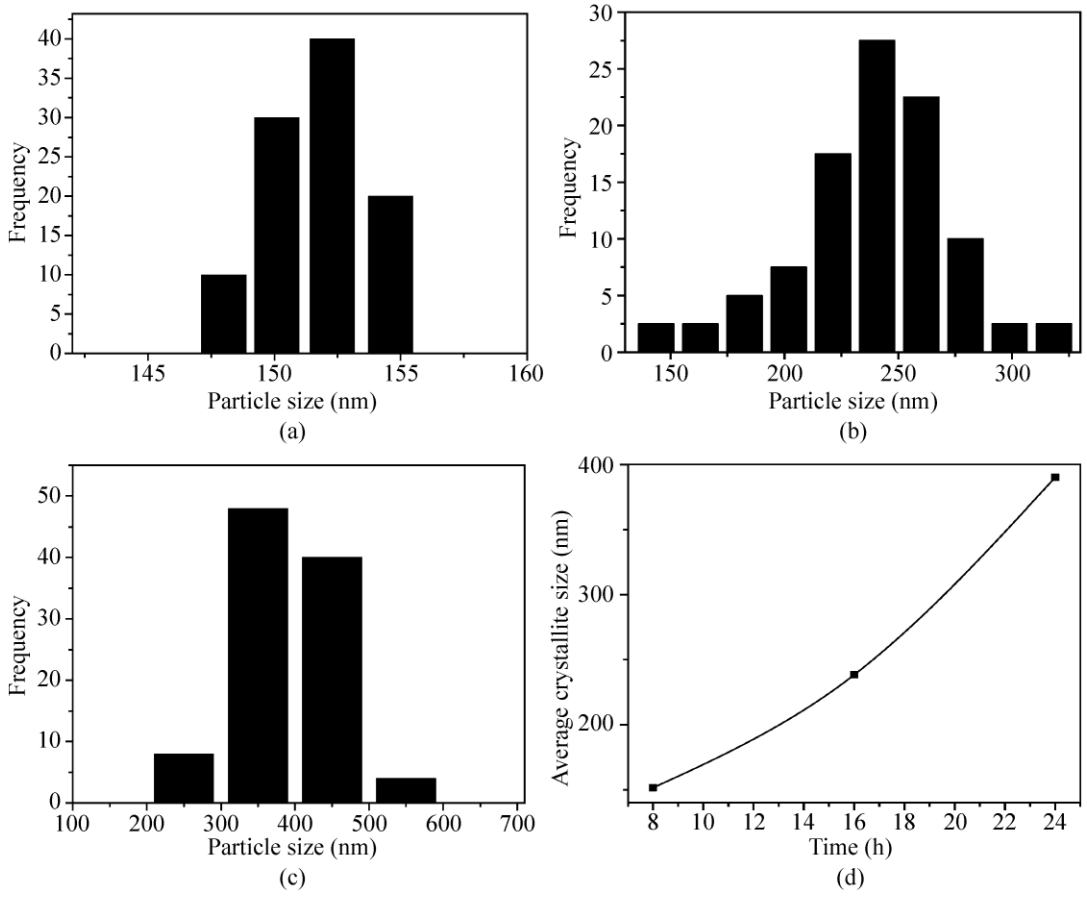

Figure 4 Histograms of the particle size distribution of the products obtained by reaction at 150 °C for (a) 8, (b) 16, (c) 24 h, and (d) the variation of average crystallite size with $MnSO_4$ (5.6 mmol/L) and CTAB (16.7 mmol/L)

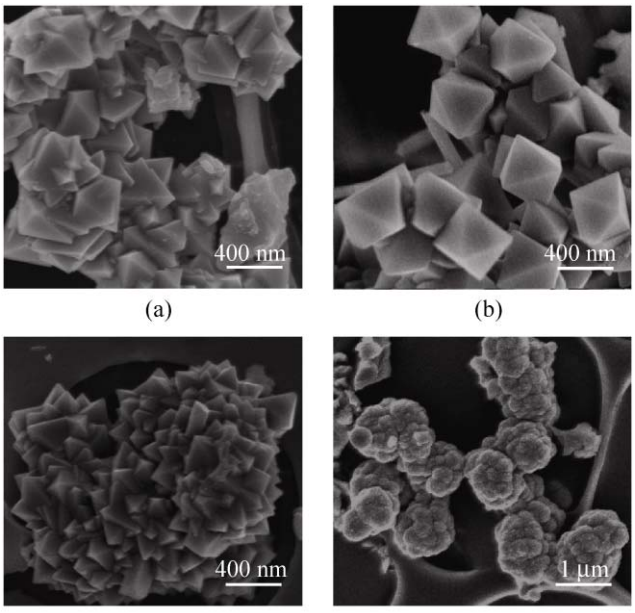

Figure 5 SEM of images of products formed with (a) [CTAB] = 33.4 mmol/L, (b) [PVP] = 0.09 mmol/L, [CTAB] = 16.7 mmol/L, (c) [PVP] = 0.63 mmol/L, (d) [P123] = 0.536 mmol/L in the presence of $MnSO_4 \cdot H_2O$ (5.6 mmol/L) at 85 ˚C for 24 h

into the polymer fiber matrices and cationic surfactant micelles, which favored gradual redispersion, as shown in Fig. 5(b). Figure 5(c) shows that particles produced using PVP alone, were all formed as large aggregates with all octahedral morphology lost. To better understand the influence of surfactants on morphology, we also used a poly(ethylene oxide) (PEO)-poly(propylene oxide) (PPO) triblock copolymer surfactant, which yielded crystallites of a quasi-spherical shape that may consist of small spheres (Fig. 5(d)).

We speculate that excess quaternary ammonium cations from CTAB are adsorbed at the negatively charged positions of the gap of the particle surface, while the hydrophobic groups extend into the aqueous phase, decreasing the hydrophilicity of the gap of the particle surface, inducing a negative capillary force, and blocking liquid permeation. In the CTAB/PVP system, a PVP–metal interaction occurs through the carbonyl group of the pyrrolidone ring during the process of further growth [35, 36], which increases the repulsion energy and decreases van der Waals attractions, leading to increase of the steric hindrance between the well-defined nanocrystal structures. The polymer fiber matrices act as a stabilizing agent [37], which might control the growth rate along the lowest surface energy plane, indexed as (111). Furthermore, the P123 polyol-polymer may have dispersed around the Mn_3O_4, inducing hydrophilic groups that could interact together to form the quasi-spherical shape.

To further understand the relationship between the manganese source and the final morphology, we investigated $MnSO_4 \cdot H_2O$, $MnCl_2 \cdot 4H_2O$, and a Mn–oleate complex as manganese sources. Figure 6(a) shows that aggregates with a flower-like morphology based on octahedra, result from only a slight increase in the concentration of $MnSO_4$ compared with that used to prepare the sample shown in Fig. 1. A somewhat higher concentration of Mn^{2+} therefore prohibits the formation of the well-formed octahedral nanocrystals. Using $MnCl_2 \cdot 4H_2O$ in place of $MnSO_4 \cdot H_2O$ resulted in the formation of only some bulk particles with amorphous morphology (Fig. 6(b)), which indicated that SO_4^{2-} ions favored the construction of the octahedral shape, while Cl^- ions inhibited that process. The shape-controlled nanostructure formed in the synthesis of iron oxide also shows a dependence on the nature of the anions present [38]. A mixture of nanorods and polyhedra were formed (Fig. 6(c)) when a Mn–oleate complex dissolved in 5 mL cyclohexane and 5 mL benzyl alcohol was used as the manganese source. In summary, different manganese sources influenced the shape of the nanostructures formed.

The Mn_3O_4 with the morphology shown in Fig. 1(a) were tested for their catalytic performance in the oxidation of methylene blue in wastewater. The test conditions were Mn_3O_4 (0.02 g), MB (100 mg/L, 20 mL), and H_2O_2 (15 mL, 30 wt.%) at 80 ˚C. The spectrum at $t = 0$ was obtained for a starting solution of MB with a concentration of 20 mg/L (without Mn_3O_4 and H_2O_2). The intensities of the peaks at 614 and 664 nm were reduced after reaction for only 5 min. The MB bands at 292 and 245 nm were masked by the strong absorption of hydrogen peroxide in the range 185–300 nm. As the reaction time progressed, the reaction solution gradually turned colorless, apparently without any other side reactions, as shown in Fig. 7 by the UV–vis absorption curves recorded at different times. The degree of decolorization was expressed as $(I_0 - I)/I_0$, where I_0 is the absorption at $t = 0$ and I is the

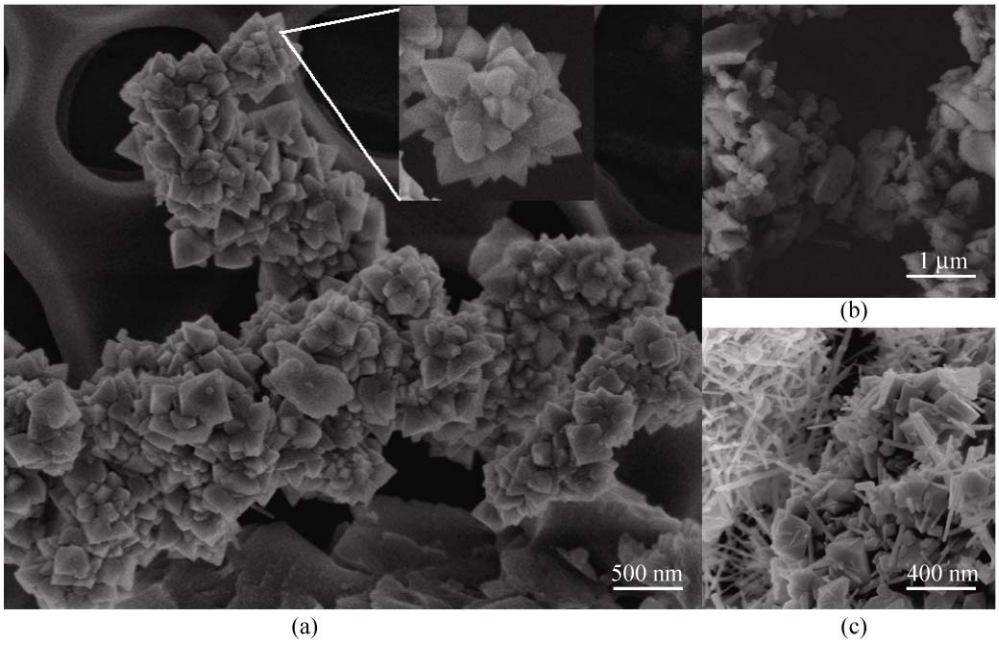

Figure 6 SEM images of the product formed with (a) $MnSO_4$ (6.9 mmol/L) and CTAB (16.7 mmol/L) at 85 ˚C for 24 h, (b) $MnCl_2$ (5.6 mmol/L) and CTAB (16.7 mmol/L) at 85 ˚C for 24 h, (c) an Mn–oleate complex (5.6 mmol/L) was dissolved in 5 mL of cyclohexane and 5 mL benzyl alcohol, and CTAB (16.7 mmol/L) was dispersed in 190 mL distilled water at 85 ˚C for 24 h

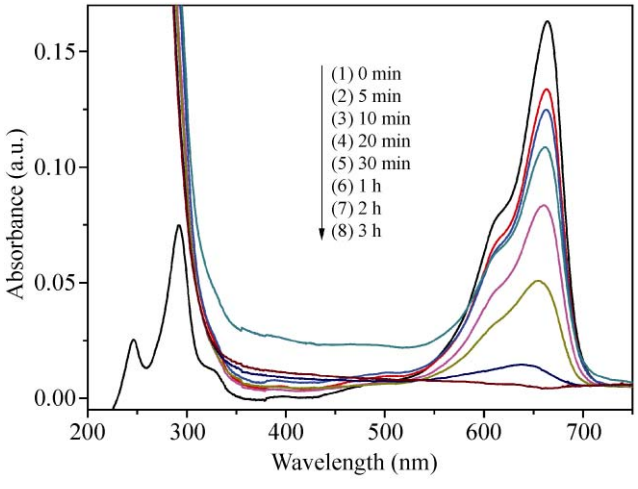

Figure 7 Absorption spectra of a solution of methylene blue (100 mg/L, 20 mL) in the presence of Mn_3O_4 octahedra (0.02 g) with the morphology shown in Fig. 1(a) and H_2O_2 (15 mL, 30 wt.%) treated at 80 ˚C for different time intervals (min) of (1) 0, (2) 5, (3) 10, (4) 20, (5) 30, (6) 60, (7) 120, (8) 180

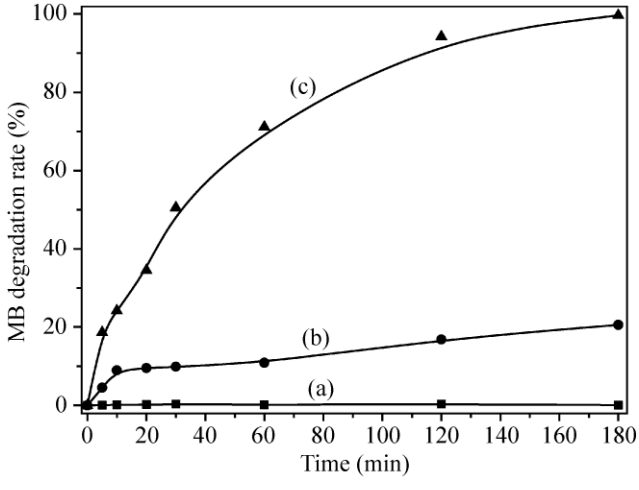

Figure 8 Time profiles of MB degradation: (a) Mn_3O_4 with the morphology shown in Fig. 1(a) + MB at 80 ˚C; (b) H_2O_2 + MB at 80 ˚C; (c) Mn_3O_4 with the morphology shown in Fig. 1(a) + MB + H_2O_2 at 80 ˚C

absorption at a given reaction time. In the absence of H_2O_2 (only MB + Mn_3O_4) or catalyst (only MB + H_2O_2), no obvious dye decolorization was observed after 3 h (curves (a) and (b) in Fig. 8). In the presence of Mn_3O_4 and H_2O_2 at 80 ˚C for 3 h, degradation of more than 99.7% of the methylene blue occurred as a result of the synergistic effect of Mn_3O_4 and H_2O_2.

4. Conclusions

We have successfully synthesized shape-controlled nanocrystals by a simple one-pot pathway, using surfactants such as CTAB, PVP, and P123 as structure-directing agents and manganese sulfate ($MnSO_4 \cdot H_2O$) as the source of manganese. The size

and shape of the nanocrystals were easily controlled by varying the synthetic parameters. When the reaction temperature was 75 ℃, only particles with an amorphous morphology were formed. When temperature was increased from 85 ℃ to 150 ℃, well-defined octahedral Mn_3O_4 nanocrystals were constructed. The average crystallite sizes increased from 152 nm to 238 nm and to 390 nm with reaction times of 8 h, 16 h, and 24 h, respectively. The mixed surfactant CTAB/PVP was effective as it could be gradually well redispersed, whilst nanocrystals were transformed into sphere-like shapes in the presence of P123. When the manganese source was changed, the crystal morphology was altered. This simple one-pot pathway should also be applicable to the preparation of other transition metal oxide nanocrystals because of its simplicity and the mild reaction conditions. As shown by application in the catalytic oxidation of methylene blue, the octahedral Mn_3O_4 nanostructures possessed a capacity for very high (above 99.7%) degradation of MB.

Acknowledgements

We gratefully acknowledge Dr. Qunli Tang (SEM), Dr. Xinqi Zhao (TEM and HRTEM), and Prof. Ronghua Yang for useful discussions. This work was financially supported by the Chinese Ministry of Science and Technology (Project Nos. 2006BAE02B05 and 2005CB221406).

References

[1] Han, Y. F.; Chen, F. X.; Zhong, Z. Y.; Ramesh, K.; Chen, L. W.; Widjaja, E. Controlled synthesis, characterization, and catalytic properties of Mn_2O_3 and Mn_3O_4 nanoparticles supported on mesoporous silica SBA-15. *J. Phys. Chem. B* **2006**, *110*, 24450–24456.

[2] Tian, Z. R.; Tong, W.; Wang, J. Y.; Duan, N. G.; Krishnan, V. V.; Suib, S. L. Manganese oxide mesoporous structures: Mixed-valent semiconducting catalysts. *Science* **1997**, *276*, 926–929.

[3] Baldi, M.; Finocchio, E.; Milella, F.; Busca, G. Catalytic combustion of C3 hydrocarbons and oxygenates over Mn_3O_4. *Appl. Catal. B: Environ.* **1998**, *16*, 43–51.

[4] Marbán, G.; Solís, T. V.; Fuertes, A. B. Mechanism of low-temperature selective catalytic reduction of NO with NH_3 over carbon-supported Mn_3O_4—role of surface NH_3 species: SCR mechanism. *J. Catal.* **2004**, *226*, 138–155.

[5] Yamashita, T.; Vannice, A. Temperature-programmed desorption of NO adsorbed on Mn_2O_3 and Mn_3O_4. *Appl. Catal. B: Environ.* **1997**, *13*, 141–155.

[6] Edwards, H. W.; Harrison, R. M. Catalysis of NO decomposition by Mn_3O_4. *Environ. Sci. Technol.* **1979**, *13*, 673–676.

[7] Wang, Y. G.; Cheng, L.; Li, F.; Xiong, H. M.; Xia, Y. Y. High electrocatalytic performance of Mn_3O_4/mesoporous carbon composite for oxygen reduction in alkaline solutions. *Chem. Mater.* **2007**, *19*, 2095–2101.

[8] Oaki, Y.; Imai, H. One-pot synthesis of manganese oxide nanosheets in aqueous solution: Chelation-mediated parallel control of reaction and morphology. *Angew. Chem. Int. Ed.* **2007**, *46*, 4951–4955.

[9] Salazar-Alvarez, G.; Sort, J.; Suriñach, S.; Baró, M. D.; Nogués, J. Synthesis and size-dependent exchange bias in inverted core–shell MnO/Mn_3O_4 nanoparticles. *J. Am. Chem. Soc.* **2007**, *129*, 9102–9108.

[10] Ahmad, T.; Ramanujachary, K. V.; Lofland, S. E.; Ganguli, A. K. Nanorods of manganese oxalate: A single source precursor to different manganese oxide nanoparticles (MnO, Mn_2O_3, Mn_3O_4). *J. Mater. Chem.* **2004**, *14*, 3406–3410.

[11] Wang, D. S.; Xie, T.; Peng, Q.; Zhang, S. Y.; Chen, J.; Li, Y. D. Direct thermal decomposition of metal nitrates in octadecylamine to metal oxide nanocrystals. *Chem. Eur. J.* **2008**, *14*, 2507–2513.

[12] Sun, X.; Zhang, Y. W.; Si, R.; Yan, C. H. Metal (Mn, Co, and Cu) oxide nanocrystals from simple formate precursors. *Small* **2005**, *1*, 1081–1086.

[13] Jiao, F.; Harrison, A.; Bruce, P. G. Ordered three-dimensional arrays of monodispersed Mn_3O_4 nanoparticles with a core–shell structure and spin-glass behavior. *Angew. Chem. Int. Ed.* **2007**, *46*, 3946–3950.

[14] Rockenberger, J.; Scher, E. C.; Alivisatos, A. P. A new nonhydrolytic single-precursor approach to surfactant-capped nanocrystals of transition metal oxides. *J. Am. Chem. Soc.* **1999**, *121*, 11595–11596.

[15] Wang, W. Z.; Ao, L. Synthesis and optical properties of Mn_3O_4 nanowires by decomposing $MnCO_3$ nanoparticles in flux. *Cryst. Growth Des.* **2008**, *8*, 358–362.

[16] Jiao, F.; Harrison, A.; Hill, A. H.; Bruce, P. G. Mesoporous Mn_2O_3 and Mn_3O_4 with crystalline walls. *Adv. Mater.* **2007**, *19*, 4063–4066.

[17] Yu, T.; Moon, J.; Park, J.; Park, Y. I.; Na, H. B.; Kim, B. H.; Song, I. C.; Moon, W. K.; Hyeon, T. Various-shaped uniform Mn_3O_4 nanocrystals synthesized at low temperature in air atmosphere. *Chem. Mater.* **2009**, *21,* 2272–2279.

[18] Shanmugam, S.; Gedanken, A. Easy single-step route to manganese oxide nanoparticles embedded in carbon and their magnetic properties. *J. Phys. Chem. C* **2008**, *112,* 15752–15758.

[19] Rusakova, I.; Ely, T. O.; Hofmann, C.; Prieto-Centurión, D.; Levin, C. S.; Halas, N. J.; Lüttge, A.; Whitmire, K. H. Nanoparticle shape conservation in the conversion of MnO nanocrosses into Mn_3O_4. *Chem. Mater.* **2007**, *19*, 1369–1375.

[20] Lei, S. J.; Tang, K. B.; Fang, Z.; Zheng, H. G. Ultrasonic-assisted synthesis of colloidal Mn_3O_4 nanoparticles at normal temperature and pressure. *Cryst. Growth Des.* **2006**, *6*, 1757–1760.

[21] Seo, W. S.; Jo, H. H.; Lee, K.; Kim, B.; Oh, S. J.; Park, J. T. Size-dependent magnetic properties of colloidal Mn_3O_4 and MnO nanoparticles. *Angew. Chem. Int. Ed.* **2004**, *43*, 1115–1117.

[22] Toberer, E. S.; Seshadri, R. Template-free routes to porous inorganic materials. *Chem. Commun.* **2006**, 3159–3165.

[23] Feldmann, C. Polyol-mediated synthesis of nanoscale functional materials. *Solid State Sciences* **2005**, *7*, 868–873.

[24] Casula, M. F.; Loche, D.; Marras, S.; Paschina, G.; Corrias, A. Role of urea in the preparation of highly porous nanocomposite aerogels. *Langmuir* **2007**, *23*, 3509–3512.

[25] Koebel, M.; Strutz, E. O. Thermal and hydrolytic decomposition of urea for automotive selective catalytic reduction systems: Thermochemical and practical aspects. *Ind. Eng. Chem. Res.* **2003**, *42*, 2093–2100.

[26] Kaminskaia, N. V.; Kostic, N. M. Kinetics and mechanism of urea hydrolysis catalyzed by palladium(II) complexes. *Inorg. Chem.* **1997**, *36*, 5917–5926.

[27] Alexandrova, A. N.; Jorgensen, W. L. Why urea eliminates ammonia rather than hydrolyzes in aqueous solution. *J. Phys. Chem. B* **2007**, *111*, 720–730.

[28] An, K.; Lee, N.; Park, J.; Kim, S. C.; Hwang, Y.; Park, J. G.; Kim, J. Y.; Park, J. H.; Han, M. J.; Yu J.; Hyeon, T. Synthesis, characterization, and self-assembly of pencil- shaped CoO nanorods. *J. Am. Chem. Soc.* **2006**, *128,* 9753–9760.

[29] Gorbenkoa, O. Y.; Graboya, I. E.; Amelicheva, V. A.; Bosaka, A. A.; Kaula, A. R.; Güttlerb, B.; Svetchnikovc, V. L.; Zandbergen, H. W. The structure and properties of Mn_3O_4 thin films grown by MOCVD. *Solid State Commun.* **2002**, *124*, 15–20.

[30] Cheng, F. Y.; Chen, J.; Gou, X. L.; Shen, P. W. High-power alkaline Zn–MnO_2 batteries using γ-MnO_2 nanowires/nanotubes and electrolytic zinc powder. *Adv. Mater.* **2005**, *17*, 2753–2756.

[31] Li, Y. G.; Wu, Y. Y. Formation of $Na_{0.44}MnO_2$ nanowires via stress-induced splitting of birnessite nanosheets. *Nano. Res.* **2009**, *2*, 54–60.

[32] Penland, R. B.; Mizushima, S.; Curran, C.; Quagliano, J. V. Infrared absorption spectra of inorganic coordination complexes. X. Studies of some metal–urea complexes. *J. Am. Chem. Soc.* **1957**, *79*, 1575–1578.

[33] Braun, A.; Ilavsky, J.; Dunn, B. C.; Jemian, P. R.; Huggins, F. E.; Eyring, E. M.; Huffman, G. P. Ostwald ripening of cobalt precipitates in silica aerogels? An ultra-small-angle X-ray scattering study. *J. Appl. Cryst.* **2005**, *38*, 132–138.

[34] Liu, B.; Zeng, H. C. Symmetric and asymmetric Ostwald ripening in the fabrication of homogeneous core–shell semiconductors. *Small* **2005**, *1*, 566–571.

[35] Lu, X. F.; Zhao, Y. Y.; Wang, C. Fabrication of PbS nanoparticles in polymer-fiber matrices by electrospinning. *Adv. Mater.* **2005**, *17*, 2485–2488.

[36] Tsuji, M.; Hashimoto, M.; Nishizawa, Y.; Kubokawa, M.; Tsuji, T. Microwave-assisted synthesis of metallic nano-structures in solution. *Chem. Eur. J.* **2005**, *11*, 440–452.

[37] Biener, J.; Nyce, G. W.; Hodge, A. M.; Biener, M. M.; Hamza, A. V.; Maier, S. A. Nanoporous plasmonic metamaterials. *Adv. Mater.* **2008**, *20*, 1211–1217.

[38] Jia, C. J.; Sun, L. D.; Luo, F.; Han, X. D.; Heyderman, L. J.; Yan, Z. G.; Yan, C. H.; Zheng, K.; Zhang, Z.; Takano, M., et al. Large-scale synthesis of single-crystalline iron oxide magnetic nanorings. *J. Am. Chem. Soc.* **2008**, *130*, 16968–16977.